

# OVERVIEW AND APPLICATIONS OF UAVSAR's MULTI-SQUINT POLARIMETRIC IMAGING MODE

Scott Hensley, Curtis Chen, Thierry Michel, Cathleen Jones, Bruce Chapman, and Ron Muellerschoen

*Jet Propulsion Laboratory, California Institute of Technology, 4800 Oak Grove Dr, Pasadena, CA 91109*

## ABSTRACT

NASA's Jet Propulsion Laboratory has developed a re-configurable polarimetric L-band synthetic aperture radar (SAR), specifically designed to acquire airborne repeat track interferometric (RTI) SAR data for application to monitoring surface deformation and vegetation structure measurements. The system employs a precision autopilot developed by NASA Dryden that allows the plane to fly precise trajectories usually within a 5 m tube. Also required for robust repeat pass applications is the ability to point the antenna in the same direction on repeat passes to a fraction of an azimuth beamwidth ( $8^\circ$  for UAVSAR). This precise pointing is achieved using an electronically scanned antenna whose pointing is based on inertial navigation unit (INU) attitude angle data. The radar design is fully polarimetric with an 80 MHz bandwidth (2 m range resolution) and has a greater than 20 km range swath when flying at its nominal altitude of 12500 m. The ability to electronically steer the beam on a pulse-to-pulse basis has allowed a new mode of SAR data acquisition whereby the radar beam is steered to different squint angles on successive pulses thereby simultaneously generating images at multiple squint angles. This mode offers the possibility of generating vector deformation measurements with a single pair of repeat passes and to obtain greater  $k_z$  diversity for vegetation studies with a reduced number of passes. This paper will present an overview of the mode, discuss its potential for deformation and vegetation, and show some examples using UAVSAR data.

Key words: UAVSAR, multisquint, interferometry, radar, troposphere.

## 1. INTRODUCTION

Repeat pass radar interferometry has become one of the key tools for mapping surface deformation either from natural or anthropogenic causes. By collecting data at times spanning a signal of interest, deformation along the radar line-of-sight can be measured with millimeter precision [3]. Since surface deformation is three dimensional, multiple vantage observations are required in order to fully solve for the deformation vector. In general



*Figure 1. Modified NASA Gulfstream III in early flight tests with the UAVSAR pod attached to the underside of the aircraft. Photo courtesy of NASA Dryden Flight Research Center.*

this requires a minimum of three interferometric pairs with suitable viewing geometries to obtain a solution. Thus, obtaining full vector deformation measurements puts considerable resource constraints on a radar observing system to make such measurements and any technique that would reduce the required number of repeat passes could prove beneficial.

The two largest sources of error in radar interferometric deformation measurements from a well designed system are the phase noise resulting from temporal decorrelation and the atmospheric phase noise due mainly to tropospheric water vapor changes between observations. Current strategies for mitigating tropospheric distortions to the phase can be roughly grouped into three categories. The first strategy basically assumes the atmospheric noise is random between interferometric pairs and reduces the noise by the square root of the number of interferometric observations. Since collecting enough pairs for this to be viable for reducing typical levels of atmospheric noise can take months while the surface is still deforming, strategies such as a permanent scatterer techniques are used to separate out the signal from atmospheric noise. A second class of techniques uses estimates of the amount of tropospheric water vapor based on ancillary sensor data such as that provided by MODIS or GPS. These techniques have proved useful when data is available but usually have resolutions much less than radar systems mak-

ing the deformation measurements. Finally, numerical weather models are being applied to estimate the tropospheric signature. None of the aforementioned techniques makes a direct measurement of the atmospheric noise coincident with the radar observations.

To overcome both the problem of obtaining vector deformation measurements on the same pass while simultaneously estimating the atmospheric noise, multi-squint observations were proposed in [1]. In this paper we examine via simulation and real data the efficacy of the multi-squint mode for obtaining vector deformation estimates along with an estimate of the atmospheric phase using UAVSAR's multi-squint mode.

## 2. UAVSAR OVERVIEW

UAVSAR is a NASA/JPL L-band fully polarimetric synthetic aperture radar employing an electronically scanned array whose primary design goal was to enable robust repeat pass radar interferometric measurements of deforming surfaces either from natural or anthropogenic causes. The radar is housed in a pod mounted to the fuselage of a Gulfstream III jet as shown in Figure 1. Nominally, the aircraft flies at an altitude of 12.5 km and maps a 22 km swath with incidence angles ranging from 25° to 60°. The 80 MHz range bandwidth results in single look complex imagery (SLC) with range and azimuth resolutions of 1.66 m and 1 m respectively. Electronic steering of the antenna is tied to the inertial navigation unit so that consistent pointing is achieved regardless of the platform yaw. The platform was modified to include a precision autopilot (PPA) that allows the aircraft to fly a specified trajectory within a 5 m tube [2]. Radar signal history and ancillary navigation data are recorded to a 1.8 TB RAID array and transferred to high density discs for transport to JPL. Processing of the data is done at JPL and then archived at the Alaska Satellite Facility (ASF) where investigators can retrieve image products.

UAVSAR has an electronically scanned antenna that can be steered on every pulse in increments of approximately 0.25°. By steering the beam on successive pulses to three steering angles located fore, broadside and aft of the aircraft trajectory as shown in Figure 2 it is possible to collect time-multiplexed imagery with three squint angles on a single pass. As with polarimetry, the PRF must be increased by a factor of three to avoid spectral aliasing. Since the UAVSAR antenna can be steered to about 25° without loss in polarimetric performance it is possible to collect fully polarimetric data (PRF must be increased by a factor of 6 in this case) with an azimuth angle spread of up to 50°. To date most of the multi-squint collections have had azimuth angles between  $\pm 5^\circ$  and  $\pm 20^\circ$  relative to zero-Doppler and have been collected at our calibration site located on the Rosamond Dry Lake Bed near the NASA Dryden facility in California.

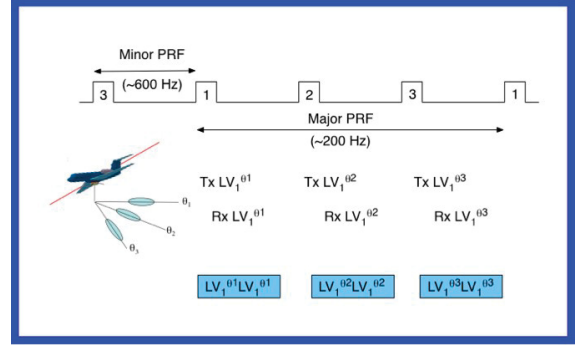


Figure 2. Figure showing the radar pulse timing for UAVSAR's experimental multi-squint mode.

## 3. VECTOR DEFORMATION

Line-of-sight measurements made from interferometric phase measurements are the most sensitive way to measure surface deformation. To obtain full vector deformation measurements, multiple measurements from different line-of-sights are combined to give the deformation vector in the desired reference frame. The vector displacement,  $\vec{d}$ , in terms of a specified set of basis vectors  $\hat{e}_i, i = 1, 3$  is given by

$$\vec{d} = \sum_{i=1}^3 d_i \hat{e}_i = \sum_{i=1}^3 \langle \vec{d}, \hat{e}_i \rangle \hat{e}_i. \quad (1)$$

Deformation measurements can also be made based on image offsets between two SAR images. Offsets can be a valuable source of surface deformation for places in the interferogram that are too decorrelated to retrieve useful deformation measurements, *e.g.*, major surface disruption due to an earthquake, or to determine 3-D vector displacements when sufficient multiple line-of-sight interferometric measurements are not available. Displacement accuracy in the line-of-sight and cross line-of-sight are given by

$$\sigma_\rho = \frac{\sqrt{3}}{\pi} \frac{1}{\sqrt{2W_\rho W_s}} \sqrt{\frac{1 - \gamma_e^2}{\gamma_e^2}} \Delta\rho \quad (2)$$

$$\sigma_s = \frac{\sqrt{3}}{\pi} \frac{1}{\sqrt{2W_\rho W_s}} \sqrt{\frac{1 - \gamma_e^2}{\gamma_e^2}} \Delta s \quad (3)$$

where  $W_\rho$  and  $W_s$  are the window dimensions used for image cross correlation and  $\Delta\rho$  and  $\Delta s$  are the range and azimuth resolutions respectively and  $\gamma_e$  is the effective correlation after any spectral filtering.

Suppose we have  $N$  deformation observations,  $o_j, j = 1, N$ , along lines-of-sight,  $\hat{\ell}_j$ , which using Equation 1 can be written as

$$o_j = \langle \vec{d}, \hat{\ell}_j \rangle = \sum_{i=1}^3 d_i \langle \hat{\ell}_j, \hat{e}_i \rangle \quad (4)$$

and can be a combination of phase and offset measurements. Hence, the sensitivity of the  $i^{\text{th}}$  component of the deformation,  $d_i$ , is

$$\frac{\partial o_j}{\partial d_i} = \langle \hat{\ell}_j, \hat{e}_i \rangle. \quad (5)$$

Letting  $\vec{o}$  be the vector of observations, then from Equation 5 we have the matrix equation

$$\vec{o} = \begin{bmatrix} \langle \vec{d}, \hat{\ell}_1 \rangle \\ \vdots \\ \langle \vec{d}, \hat{\ell}_N \rangle \end{bmatrix}_{N \times 1} = A \vec{d} = \begin{bmatrix} \langle \hat{\ell}_1, \hat{e}_1 \rangle & \langle \hat{\ell}_1, \hat{e}_2 \rangle & \langle \hat{\ell}_1, \hat{e}_3 \rangle \\ \vdots & \vdots & \vdots \\ \langle \hat{\ell}_N, \hat{e}_1 \rangle & \langle \hat{\ell}_N, \hat{e}_2 \rangle & \langle \hat{\ell}_N, \hat{e}_3 \rangle \end{bmatrix}_{N \times 3} \begin{bmatrix} d_1 \\ d_2 \\ d_3 \end{bmatrix}_{3 \times 1} \quad (6)$$

This is a classical least squares problem with solution

$$\vec{d} = (A^T Q^{-1} A)^{-1} A^T Q^{-1} \vec{o} \quad (7)$$

where  $Q$  is covariance matrix of the observations. Assuming a diagonal matrix for the observation covariance matrix with the  $j^{\text{th}}$  observation having covariance,  $\sigma_j$ , then from Equation 7 the solution of Equation 6 is

$$\vec{d} = \begin{bmatrix} \sum_{j=1}^N \frac{1}{\sigma_j^2} \langle \hat{e}_1, \hat{\ell}_j \rangle^2 & \sum_{j=1}^N \frac{1}{\sigma_j^2} \langle \hat{e}_1, \hat{\ell}_j \rangle \langle \hat{e}_2, \hat{\ell}_j \rangle & \sum_{j=1}^N \frac{1}{\sigma_j^2} \langle \hat{e}_1, \hat{\ell}_j \rangle \langle \hat{e}_3, \hat{\ell}_j \rangle \\ \sum_{j=1}^N \frac{1}{\sigma_j^2} \langle \hat{e}_2, \hat{\ell}_j \rangle \langle \hat{e}_1, \hat{\ell}_j \rangle & \sum_{j=1}^N \frac{1}{\sigma_j^2} \langle \hat{e}_2, \hat{\ell}_j \rangle^2 & \sum_{j=1}^N \frac{1}{\sigma_j^2} \langle \hat{e}_2, \hat{\ell}_j \rangle \langle \hat{e}_3, \hat{\ell}_j \rangle \\ \sum_{j=1}^N \frac{1}{\sigma_j^2} \langle \hat{e}_3, \hat{\ell}_j \rangle \langle \hat{e}_1, \hat{\ell}_j \rangle & \sum_{j=1}^N \frac{1}{\sigma_j^2} \langle \hat{e}_3, \hat{\ell}_j \rangle \langle \hat{e}_2, \hat{\ell}_j \rangle & \sum_{j=1}^N \frac{1}{\sigma_j^2} \langle \hat{e}_3, \hat{\ell}_j \rangle^2 \end{bmatrix}^{-1} \begin{bmatrix} \sum_{j=1}^N \frac{1}{\sigma_j^2} \langle \hat{e}_1, \hat{\ell}_j \rangle \langle \vec{d}, \hat{\ell}_j \rangle \\ \sum_{j=1}^N \frac{1}{\sigma_j^2} \langle \hat{e}_2, \hat{\ell}_j \rangle \langle \vec{d}, \hat{\ell}_j \rangle \\ \sum_{j=1}^N \frac{1}{\sigma_j^2} \langle \hat{e}_3, \hat{\ell}_j \rangle \langle \vec{d}, \hat{\ell}_j \rangle \end{bmatrix}$$

with formal covariance error of

$$\sigma_{\vec{d}} = \begin{bmatrix} \sum_{j=1}^N \frac{1}{\sigma_j^2} \langle \hat{e}_1, \hat{\ell}_j \rangle^2 & \sum_{j=1}^N \frac{1}{\sigma_j^2} \langle \hat{e}_1, \hat{\ell}_j \rangle \langle \hat{e}_2, \hat{\ell}_j \rangle & \sum_{j=1}^N \frac{1}{\sigma_j^2} \langle \hat{e}_1, \hat{\ell}_j \rangle \langle \hat{e}_3, \hat{\ell}_j \rangle \\ \sum_{j=1}^N \frac{1}{\sigma_j^2} \langle \hat{e}_2, \hat{\ell}_j \rangle \langle \hat{e}_1, \hat{\ell}_j \rangle & \sum_{j=1}^N \frac{1}{\sigma_j^2} \langle \hat{e}_2, \hat{\ell}_j \rangle^2 & \sum_{j=1}^N \frac{1}{\sigma_j^2} \langle \hat{e}_2, \hat{\ell}_j \rangle \langle \hat{e}_3, \hat{\ell}_j \rangle \\ \sum_{j=1}^N \frac{1}{\sigma_j^2} \langle \hat{e}_3, \hat{\ell}_j \rangle \langle \hat{e}_1, \hat{\ell}_j \rangle & \sum_{j=1}^N \frac{1}{\sigma_j^2} \langle \hat{e}_3, \hat{\ell}_j \rangle \langle \hat{e}_2, \hat{\ell}_j \rangle & \sum_{j=1}^N \frac{1}{\sigma_j^2} \langle \hat{e}_3, \hat{\ell}_j \rangle^2 \end{bmatrix}^{-1}$$

#### 4. DEFORMATION AND THE UAVSAR MULTI-SQUINT MODE

This section adapts the vector deformation model from Section 3 to the multi-squint imaging geometry. Consider a three beam multi-squint mode where the antenna is steered to broadside and to azimuth angles  $\pm\theta_{az}$  where the azimuth angle is the angle between broadside and the projection of the look vector into the ground plane as shown in Figure 3. The look vector to a pixel is then given by

$$\hat{\ell} = \begin{bmatrix} \sin \theta_{\ell} \sin \theta_{az} \\ \sin \theta_{\ell} \cos \theta_{az} \\ -\cos \theta_{\ell} \end{bmatrix} \quad (8)$$

where  $\theta_{\ell}$  is the look angle. Using some simple right-triangle trigonometry, the squinted look angle,  $\theta_{\ell}$ , can be related to the look angle at broadside by

$$\tan \theta_{\ell} = \frac{\tan \theta_{\ell_o}}{\cos \theta_{az}} \quad (9)$$

and from Equation 8 the cosine of the squint angle, the angle between the broadside look vector and the squinted look vector is

$$\cos \theta_{sq} = \sin \theta_{\ell} \sin \theta_{\ell_o} \cos \theta_{az} + \cos \theta_{\ell} \cos \theta_{\ell_o}. \quad (10)$$

From Figure 3 the squinted range and the range at broadside are simply related by

$$\rho_{sq} = \frac{\rho_o}{\cos \theta_{sq}}. \quad (11)$$

We can write the aft pointing look vector,  $\hat{\ell}_{-1}$ , and the forward pointing look vector,  $\hat{\ell}_1$ , in terms of the look vector at broadside,  $\hat{\ell}_o = \hat{\rho}$ , and a unit vector in the along-track direction,  $\hat{s}$ , by

$$\hat{\ell}_{-1} = \cos \theta_{sq} \hat{\rho} + \sin \theta_{sq} \hat{s} \quad (12)$$

$$\hat{\ell}_o = \hat{\rho} \quad (13)$$

$$\hat{\ell}_1 = \cos \theta_{sq} \hat{\rho} + \sin \theta_{sq} \hat{s} \quad (14)$$

So consider repeat passes in the multi-squint mode with surface deformation vector,  $\vec{d}$ , between passes. Then the interferometric phase,  $\phi_i$ , observed for each look direction,  $i = -1, 0, 1$ , is given by

$$\phi_i = \frac{4\pi}{\lambda} \left[ -\langle \vec{b}, \hat{\ell}_i \rangle + \langle \vec{d}, \hat{\ell}_i \rangle + \Delta \rho_{atm_i} \right] + \phi_{n_i} \quad (15)$$

$$= \frac{4\pi}{\lambda} \left[ d_{\rho} \cos \theta_{sq} + d_s \sin \theta_{sq} + \frac{\Delta \tilde{\rho}_{atm}}{\cos \theta_{sq}} \right] + \phi_{n_i} \quad (16)$$

where  $-\langle \vec{b}, \hat{\ell}_i \rangle$  is the topographic phase term that is assumed compensated for in passing from Equation 15 to Equation 16,  $\Delta \tilde{\rho}_{atm}$ , is the atmospheric delay at broadside that is assumed related to squinted tropospheric delay by the geometric distance scaling factor  $\frac{1}{\cos \theta_{sq}}$  [1] and  $\phi_{n_i}$  is thermal noise. Note, the atmosphere is assumed constant between squint collections in this model. Setting,  $\hat{\rho}_{\perp} = \hat{\rho} \times \hat{s}$ , then the deformation vector in terms of the basis  $\hat{\rho} \hat{s} \hat{\rho}_{\perp}$  can be expressed in components as

$$\vec{d} = [d_{\rho} \quad d_s \quad d_{\perp}]. \quad (17)$$

Since the component of the deformation in the direction of  $\hat{\rho}_{\perp}$  is perpendicular to the look vectors in the multi-squint geometry, and therefore not measurable, we define a modified deformation vector,  $\vec{D} = (d_{\rho}, d_s, d_{atm})$ , where the last component of the displacement vector is replaced by the equivalent displacement due to the differential atmosphere at broadside. Here we are effectively assuming a frozen atmosphere model that is represented

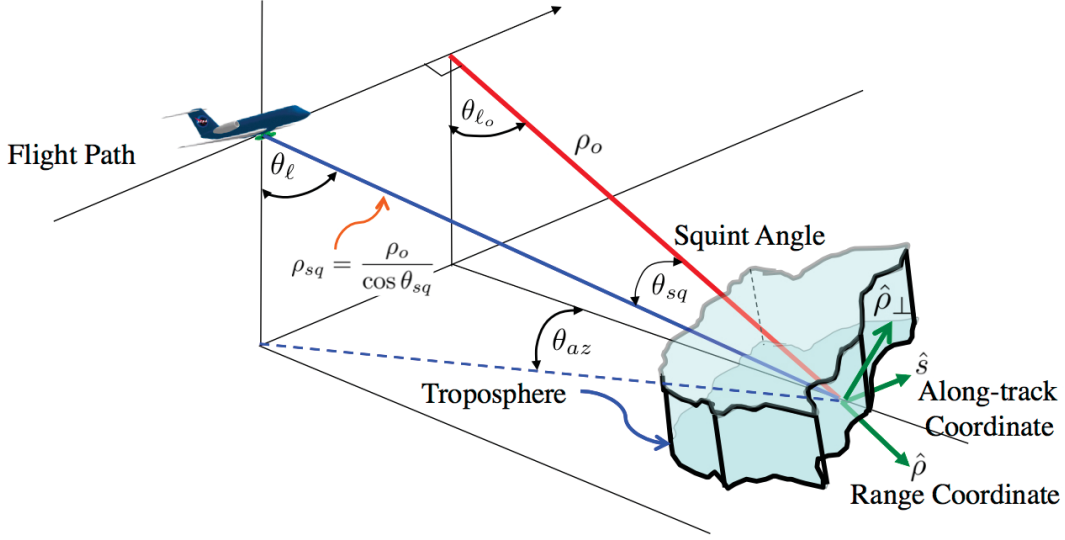


Figure 3. Figure showing UAVSAR's multi-squint imaging. The electronic beam is steered by  $\pm\theta_{az}$  off broadside and to broadside to obtain three images with different squint angles. The squint angle, the angle between the broadside line-of-sight vector and squinted line-of-sight vectors can be computed as function of the look angles and azimuth angle.

by a phase screen at the target. Limitations of these assumptions resulting from a mobile atmosphere and non-zero vertical depth are discussed in [1].

Using Equation 16 the phase measurements can be expressed in terms of the modified deformation vector by the matrix equation

$$\vec{\phi} = \frac{4\pi}{\lambda} A \vec{D} \quad (18)$$

where

$$A = \begin{bmatrix} \cos \theta_{sq} & -\sin \theta_{sq} & \frac{1}{\cos \theta_{sq}} \\ 1 & 0 & 1 \\ \cos \theta_{sq} & \sin \theta_{sq} & \frac{1}{\cos \theta_{sq}} \end{bmatrix}. \quad (19)$$

Assuming the covariance of the measurements is given by

$$Q = \frac{\lambda}{4\pi} \frac{1}{\sqrt{2N_L}} \sqrt{\frac{1-\gamma^2}{\gamma^2}} \begin{bmatrix} 1 & 0 & 0 \\ 0 & 1 & 0 \\ 0 & 0 & 1 \end{bmatrix} \quad (20)$$

where  $\gamma$  is the interferometric correlation and  $N_L$  is the number of looks, then from Equation 7 the solution to Equation 18 is

$$\begin{aligned} \vec{D} &= \begin{bmatrix} d_\rho \\ d_s \\ d_{atm} \end{bmatrix} \\ &= \begin{bmatrix} \frac{1}{4} \frac{(5+\cos(2\theta_{sq}))d_{-1}}{\sin^4 \theta_{sq}} - \frac{3}{2} \frac{d_1}{\tan^2 \theta_{sq} \sin^2 \theta_{sq}} & \frac{1}{2} \frac{d_0}{\sin^2 \theta_{sq}} \\ -\frac{3}{2} \frac{d_{-1}}{\tan^2 \theta_{sq} \sin^2 \theta_{sq}} + \frac{1}{2} \frac{(2+\cos(2\theta_{sq}))d_1}{\tan^2 \theta_{sq} \sin^2 \theta_{sq}} \end{bmatrix} \end{aligned} \quad (21)$$

where  $d_i = \frac{\lambda}{4\pi} \phi_i$  and with formal covariance matrix of the solution vector given by

$$\text{cov}_{\vec{D}} = \left( \frac{\lambda}{4\pi} \right)^2 \frac{1}{2N_L} \frac{1-\gamma^2}{\gamma^2} \begin{bmatrix} \frac{1}{4} \frac{5+\cos(2\theta_{sq})}{\sin^4(\theta_{sq})} & 0 & -\frac{3}{2} \frac{\cot^2(\theta_{sq})}{\sin^2(\theta_{sq})} \\ 0 & \frac{1}{2\sin^2(\theta_{sq})} & 0 \\ -\frac{3}{2} \frac{\cot^2(\theta_{sq})}{\sin^2(\theta_{sq})} & 0 & \frac{1}{2} \frac{(2+\cos(2\theta_{sq}))\cot^2(\theta_{sq})}{\sin^2(\theta_{sq})} \end{bmatrix}. \quad (22)$$

Figure 4 shows the expected precision of the modified deformation vector using the diagonal terms of Equation 22. The right plot in the figure shows the precision as a function of azimuth angle for a look angle of  $45^\circ$  assuming an interferometric correlation of 0.92 and the number of looks equal to 36. In the left plot the expected precision is plotted as a function of look angle for an azimuth steering angle of  $15^\circ$ . Note how steeply the precision of the range and atmosphere terms increases in the near range. This is result of the decreased squint angle in the near range as can be seen from Equation 10.

## 5. SIMULATION RESULTS

To test the efficacy of the formulation described in Section 4 for estimating the components of the modified deformation vector, we simulated a subsidence bowl in the presence of atmospheric distortion being imaged with the UAVSAR multi-squint mode with an azimuth steering angle of  $15^\circ$ . The east, north, up, *enu*, components of

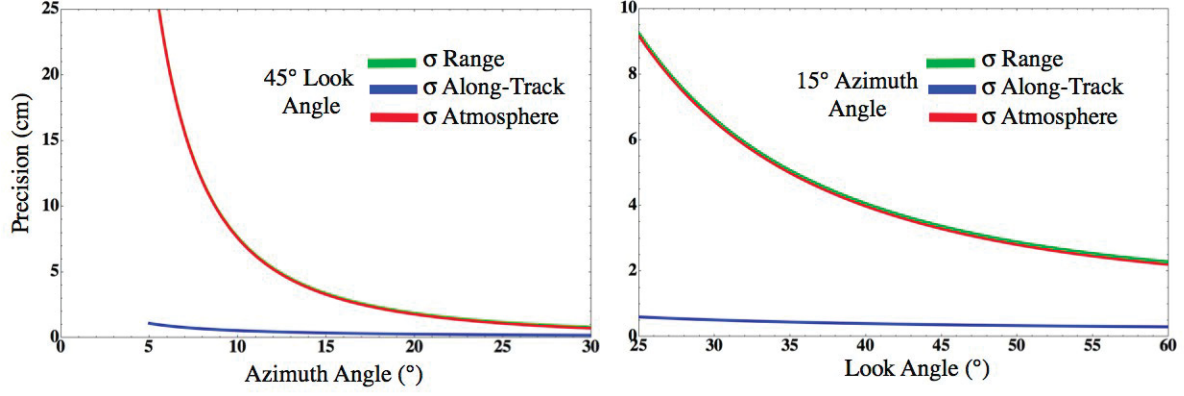


Figure 4. The left plot in the figure shows the expected precision of the modified deformation vector at a look angle of 45° as a function of azimuth angle. In the right plot is the expected precision of the modified deformation vector as a function of look angle for a 15° azimuth angle. In both cases the correlation was set to 0.92 and the number of looks to 36.

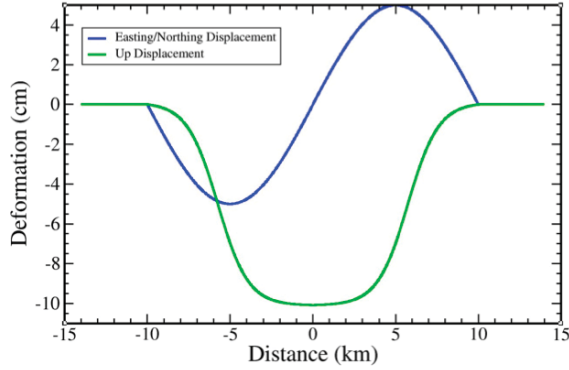


Figure 5. Cross sections of the deformation in the simulated subsidence bowl.

the subsidence bowl are given by

$$\vec{d} = \begin{bmatrix} -L_m \sin \left[ \frac{\pi(e - e_o)}{r_b} \right] \\ -L_m \sin \left[ \frac{\pi(n - n_o)}{r_b} \right] \\ \frac{(u_t - u_b)}{2 \tanh s_f} \tanh \left[ \frac{2s_f(r - r_f)}{r_b - r_f} - s_f \right] + \frac{u_t + u_b}{2} \end{bmatrix} \quad (23)$$

where  $L_m$  is the maximal planimetric displacement (5 cm),  $(e_o, n_o)$  is the center of the subsidence bowl,  $r_b$  is the radius of the subsidence bowl (10 km),  $s_f$  is a steepness factor (2.3),  $r_f$  is the radius of the flank of the bowl (1.5 km),  $u_t$  is the vertical subsidence at the edge of the bowl (0 cm) and  $u_b$  is the subsidence at the center (-10 cm). Figure 5 shows a plot of the easting/northing and up components of the deformation generated using Equation 23. Thermal noise was simulated using an interferometric correlation of 0.92 with 36 looks which corresponds to 9 mm of deformation noise. The atmosphere was simulated using a power law PSD with an exponent

of  $-\frac{8}{3}$  and with an RMS noise level of 2 cm. For the simulation we assumed the nominal UAVSAR platform height of 12.5 km with a heading of 45°. Simulated data is generated for look angles ranging from 25° to 60°.

Results of the inversion are shown in Figure 6. The top row of the figure shows the true range and along-track components of the deformation vector and the simulated phase distortion. In the bottom row are the estimated components of the modified deformation vector. As expected from the sensitivity plots in Section 4 the range and atmosphere components get much noisier in the near range whereas the along-track component has much less noise. The noise levels matched those predicted by Equation 22 extremely well. Note the mixing of the atmospheric distortion between the range and atmosphere components. Low-pass filtering the range component eliminates much of the atmospheric term and provides a good estimate of the range component of the deformation. A simple low-pass filter does not help in obtaining a better estimate of the atmosphere term and better methods for extracting this term are being investigated.

## 6. ROSAMOND LAKE BED TEST CASE

Three passes of UAVSAR multi-squint data were collected on July 20, 2010 over the Rosamond Dry Lake Bed where an array of corner reflectors is deployed for calibration purposes. Each pass was collected on a heading of 350° at the nominal flying altitude of 12500 m. The antenna was steered to azimuth angles of  $\pm 15^\circ$  and  $0^\circ$ . The repeat times between passes 1 and 2 was 26.2 min, between passes 2 and 3 was 33.3 min and between passes 1 and 3 was 51.9 min. The short temporal baseline and geologic stability of the site precludes any deformation signature, however the time interval between repeat passes is sufficient for the tropospheric water vapor to have changed resulting in atmospheric distortions to the phase.



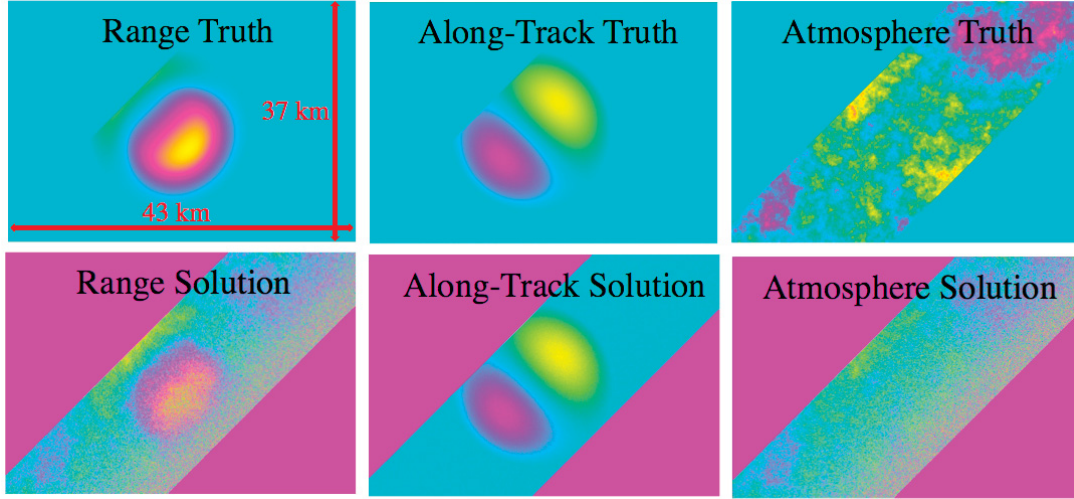


Figure 6. The top row of this figure shows the simulated deformation components in the range and along-track directions and simulated atmospheric distortion. In the bottom row are the estimated range, along-track atmospheric distortion components of the modified deformation vector. Note, the increased noise in the range and atmosphere components in the near range as was indicated in Section 4. The noise level in each component matched those predicted by Equation 22. Color contours are wrapped at 15 cm.

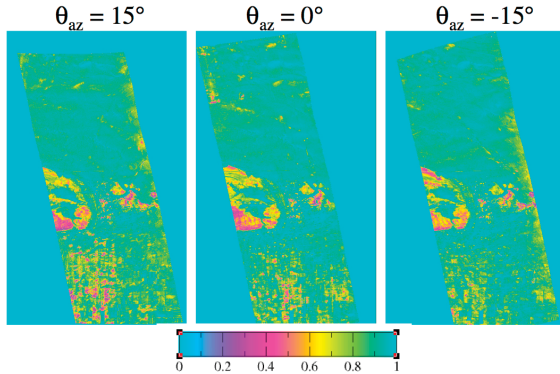


Figure 7. Correlation maps for the three squint angles for passes 1 and 2. Note the mean correlation increases with decreasing azimuth angle. Correlation maps for the other pairs were similar.

Figure 7 shows the correlation maps for passes 1 and 2 for the three squint angles. Note near range is on the right side of the image strip. Similar results were obtained for the other pairs. Note the mean correlation in the urban area at the bottom of the image increases with decreasing azimuth angle which is attributed to the better alignment of the road directions with the line-of-sight vector for the aft steering angle that results in less shadowing.

Figure 8 shows the nine interferograms formed from the three interferometric pairs and the three squint angles. The RMS phase variation of 0.4 rad for the interfero-

grams formed from passes 1 and 2 that have the shortest temporal baseline is about a factor of two smaller than the other pairs. Differences in the atmospheric phase screen between squint angles are readily apparent indicating atmospheric changes during the approximately 45 second interval between the fore and aft acquisitions. Also, observe the similarity of the atmospheric phase screens for pairs 2 and 3 and 1 and 3 indicating the state of the tropospheric water vapor during the third pass dominates the phase screen.

Inverting the multi-squint interferometric data for passes 1 and 2 gives the range, along-track and atmospheric deformation components shown in Figure 9. Observe that the retrieved vector deformation layers are non-zero as would be expected for this observing scenario. We suspect that this is a combination of two factors. First, as can be seen in the raw interferograms the atmospheric phase screen is moving between the imaging times. Moreover, the movement is not just a simple translation but exhibits differences at intermediate spatial scales. This may be the result of atmospheric mixing between image acquisitions or the fact the vertical structure in the distribution of water vapor in the troposphere results in phase differences in the interferograms that do not match the model in Equations 18 and 19.

## 7. CONCLUSIONS

Estimating vector deformation normally requires interferometric observations from multiple vantages and is hampered by the presence of atmospheric noise. Using multi-

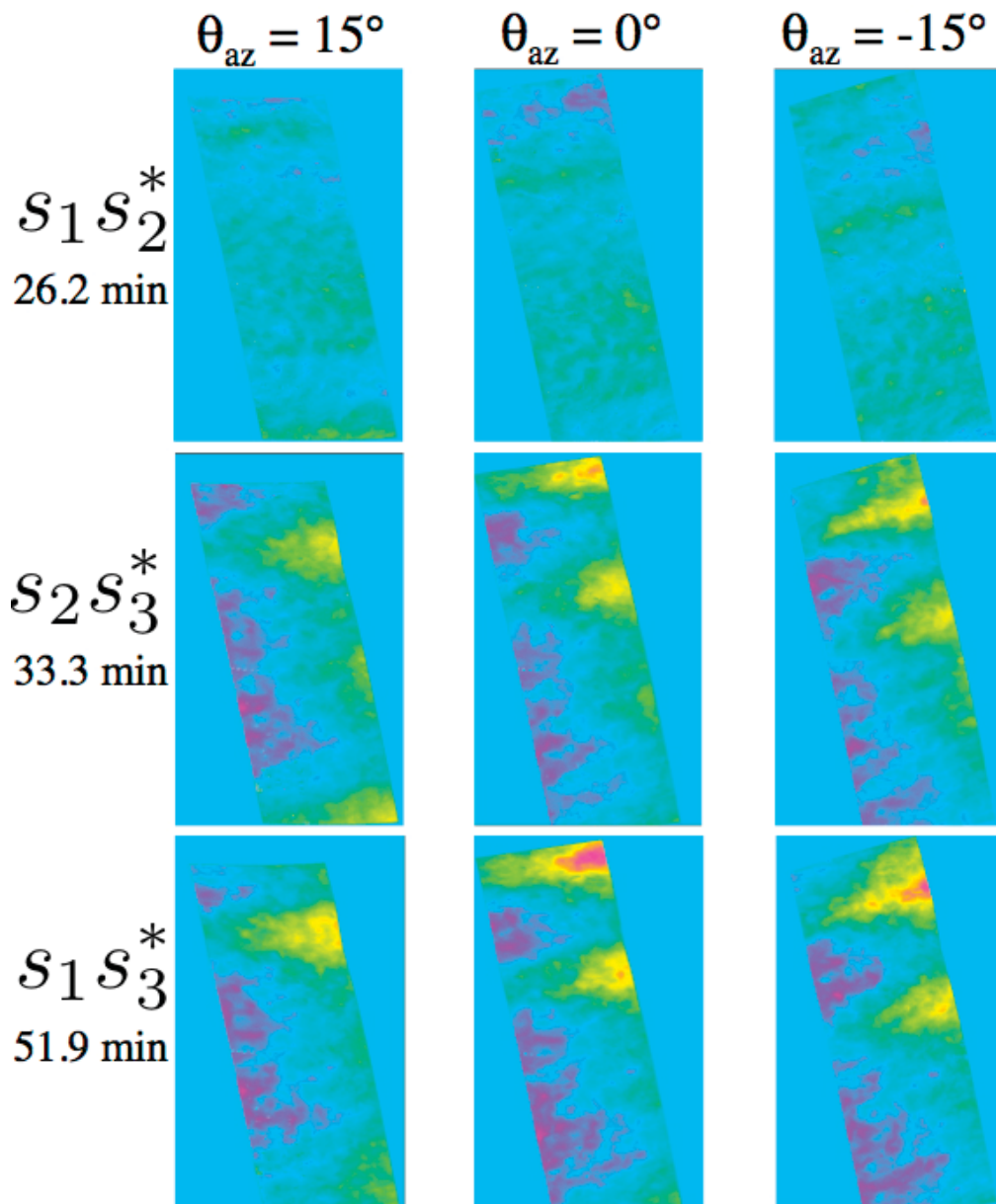


Figure 8. Interferograms for the three squint angles and three pair of passes collected on July 10, 2010 at Rosamond Dry Lake Bed. The temporal baseline for the pairs varied from 26 to 52 minutes. The RMS phase variation was about a factor of two less for the smallest temporal baseline pair. Color scale is wrapped at  $2\pi$  radians.

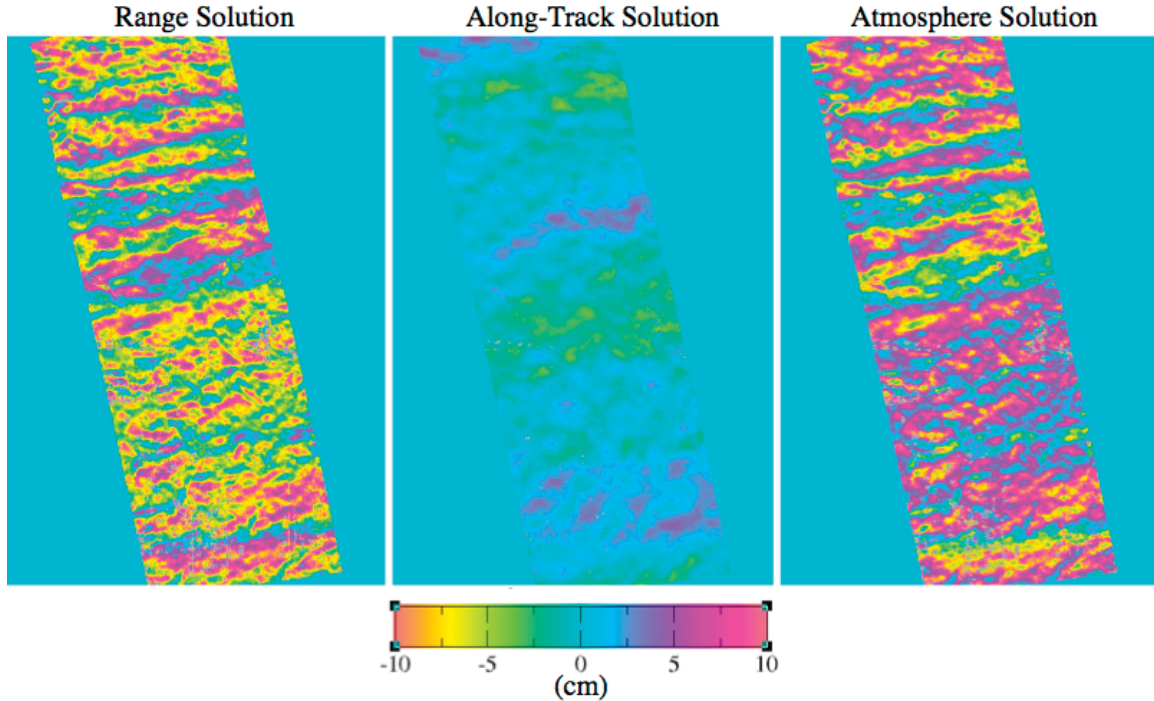


Figure 9. The retrieved vector deformation and atmosphere layers from passes 1 and 2 with the 26 minute repeat interval. We suspect that retrieved deformation being non-zero is a combination of a moving atmosphere and the non-zero vertical depth of the tropospheric water vapor.

squint data collected on a single pass it is possible to estimate two components of the deformation and the atmospheric distortion. In this paper we provided closed form expressions for both the deformation vector and its associated covariance matrix and verified these formulas with a simulation of subsidence in the presence or atmospheric distortion. We then applied this formulation to real multi-squint data collected over Rosamond Lake Bed in California. Results with real data showed in this case the combination of dynamic motion of the atmosphere between the multi-squint image acquisitions and the vertical extent of the tropospheric water vapor resulted in retrievals in which the errors in the line-of-sight deformations were not significantly reduced. More multi-squint acquisitions are needed to vet the efficacy of this mode for atmospheric mitigation.

## ACKNOWLEDGMENTS

This research was conducted at the Jet Propulsion Laboratory, California Institute of Technology, under contract with the National Aeronautics and Space Administration.

## REFERENCES

- [1] Curtis Chen. Mitigation of Tropospheric InSAR Phase Artifacts Through Differential Multisquint Processing. In *Proceeding of IGARSS 2004*, Anchorage, Alaska, July 2004.
- [2] James Lee, Brian Strovers, and Victor Lin. C-20A/GIII Precision Autopilot development in support of NASAs UAVSAR program. In *Proceeding of the NASA Science Technology Conference 2007*, Greenbelt, Maryland, June 2007. NASA.
- [3] P. A. Rosen, S. Hensley, I. R. Joughin, F. K. Li, S. N. Madsen, E. Rodriguez, and R. M. Goldstein. Synthetic Aperture Radar Interferometry. *Proc. IEEE*, 88:333–382, 2000.